Dalton Transactions

ROYAL SOCIETY OF CHEMISTRY

PAPER

View Article Online
View Journal | View Issue

Cite this: *Dalton Trans.*, 2025, **54**, 16593

Structural modifications of $M_5O_4I_{11}$ (M = Nb, Ta) cluster networks from heterogeneous solid-state reactions

Fabian Grahlow, [a] Jan Beitlberger,[a] Mario Martin,[b] Eric Juriatti,[b] Heiko Peisert, [b] Marcus Scheele, [b] Markus Ströbele, [a] Carl P. Romao[c] and Hans-Jürgen Meyer *[a]

Received 1st September 2025,
Accepted 17th October 2025

DOI: 10.1039/d5dt02097b

rsc.li/dalton

The cluster compounds $M_5O_4I_{11}$ (M = Nb, Ta) and $Ta_5O_4I_{11}(TaI_5)$ were obtained from heterogeneous solid-state reactions and structurally characterised by single-crystal X-ray diffraction. Their crystal structures are based on the novel $[M_5O_4]$ cluster core with metal (M) atoms arranged following the motif of a square pyramid. Iodide ligands contribute to different connectivities in the structures, resulting in (van der Waals type) waved layer structures. Two structural modifications exist for $Ta_5O_4I_{11}$, denoted as o-$Ta_5O_4I_{11}$ and m-$Ta_5O_4I_{11}$, and the compound $Ta_5O_4I_{11}(TaI_5)$ encloses $[TaI_5]$ molecules within voids of the structure. The two-dimensional nature of the structures and the presence of metal-to-metal bonding motivated investigations of the electronic properties through optical band-gap measurements, electrical conductivity studies, electronic band structure calculations, and X-ray photoelectron spectroscopy.

Introduction

The chemistry of reduced niobium and tantalum halides is characterised by metal cluster compounds that are usually achieved through solid-state synthesis at elevated temperatures.[1] These compounds display a wide range of structural motifs and oxidation states, with a pronounced tendency to form clusters featuring octahedral M_6 (M = Nb, Ta) cores.[2] Many transition metal (M) halide (X) clusters crystallise in either the $[M_6X_{12}]$- or $[M_6X_8]$-structural types.[3–6] The $[M_6X_{12}]$ structure consists of twelve halide ligands bridging the edges of an M_6 octahedron which generally favours combinations of larger metal atoms with smaller halides. In contrast, $[M_6X_8]$ clusters, in which eight halides cap the faces of the octahedron, tend to form when smaller metal atoms are paired with larger halide ions. Due to the spatial separation of adjacent clusters by outer ligands, these crystalline materials typically exhibit semiconducting behaviour with poor electrical conductivity.[7,8] The chemistry of binary niobium halide clusters is further enriched by triangular Nb_3 clusters present in Nb_3X_8 (X = Cl, Br, I), as well as Peierls-distorted NbX_4.[9,10] Metal-rich tantalum halides exist as Ta_6X_{14}, Ta_6X_{15} and TaX_4.[5,11–15]

Beyond these well-established binary systems, the range of cluster compounds and structural diversity expands significantly in heteroanionic halides of niobium and tantalum. Among the most common examples are chalcohalides, which include M_3 clusters, such as Ta_3SBr_7 and ANb_3SBr_7 (A = Rb, Cs),[16–18] as well as M_4 clusters exhibiting planar, butterfly or tetrahedral geometries (*e.g.* Nb_4OI_{10}; $Ta_4S_9Br_8$; Ta_4SBr_{11}; $Nb_4Se_4I_4$)[19–26] Octahedral M_6 clusters are also observed, as in Nb_6I_9S.[27] A notable characteristic of these compounds is the presence of bridging halides along with the interstitial or capping atoms, which are most often chalcogenides, and rarely pnictides (Nb_4PnX_{11}, Pn = N, P; X = Cl, Br, I).[25]

Occasionally, molecular MX_5 units are found to be incorporated into a cluster network. A notable example is $Nb_7S_2I_{19}$ which can be represented as $(Nb_3SI_7)_2(NbI_5)$, emphasising the stabilisation of thermodynamically unstable NbI_5 monomers within the inorganic framework of Nb_3SI_7. This structure exemplifies a form of structural synergism, where the enclosed molecule influences the topology of the surrounding cluster framework.[28] Similarly, space-filling $[ZrCl_5]^-$ units are observed in the compound described as $Cs_3Zr_7Cl_{20}Mn$ and $[TaBr_6]^-$ units in $(Ta_6Br_{12})Br_3(TaBr_6)_{0.86}$.[29,30]

Less common is the occurrence of pentanuclear M_5 clusters. Reported examples generally fall into two categories: those composed of two different metals, which give rise to a

[a]*Section for Solid State and Theoretical Inorganic Chemistry, Institute of Inorganic Chemistry, Eberhard Karls Universität Tübingen, Auf der Morgenstelle 18, D-72076 Tübingen, Germany. E-mail: juergen.meyer@uni-tuebingen.de*
[b]*Institute of Physical and Theoretical Chemistry, Eberhard Karls Universität Tübingen, Auf der Morgenstelle 18, D-72076 Tübingen, Germany*
[c]*Department of Materials, Faculty of Nuclear Sciences and Physical Engineering, Czech Technical University in Prague, Trojanova 13, 120 00 Prague, Czech Republic*

variety of geometries, and metal halide clusters that typically adopt a square-pyramidal cluster core. The latter is commonly observed in compounds with the general formula $[M_5X_{13}]^{n-}$ (M = Mo, W, Tc; X = Cl, Br, I; n = 0, 1, 2, 3).[31–33]

Oxyiodides of niobium and tantalum are reported as MO_2I, MOI_2 and $NbOI_3$.[34–36] More recently there has been some progress in the development of metal-rich oxyiodides.[19,37] In the course of this progress, we present a new class of metal-rich oxyiodides based on a distinctive M_5 cluster motif, observed for both niobium and tantalum.

These clusters, of the general formula $M_5O_4I_{11}$ with M = Nb and Ta, are shown to exist in two polymorphic forms for tantalum (o-$Ta_5O_4I_{11}$, m-$Ta_5O_4I_{11}$), as well as in the compound $Ta_5O_4I_{11}(TaI_5)$, containing molecular $[TaI_5]$ in its structure. The syntheses and crystal structures of the compounds are reported, and their electrical conductivities and electronic structures are analysed through a combination of experimental measurements and theoretical calculations.

Experimental

Preparations

Manipulations of starting materials, such as charging the silica ampoules (estimated volume 5 cm^3) with starting materials were performed in an argon-filled glovebox (MBraun, labmaster 130, O_2 < 1 ppm, H_2O < 1 ppm).

o-$Ta_5O_4I_{11}$, m-$Ta_5O_4I_{11}$ and $Ta_5O_4I_{11}(TaI_5)$

A mixture of TaI_5 (144.8 mg, 0.178 mmol), Ta (6.1 mg, 0.03 mmol, Merck, 99.9%), Li_2O (5.1 mg, 0.169 mmol, ABCR, 96%) and Li_2CN_2 (4.6 mg, 0.085 mmol) was fused into an evacuated silica tube and heated with 0.5 K min^{-1} to 500 °C in a Simon–Müller furnace. After heating at 500 °C for 48 hours, o-$Ta_5O_4I_{11}$ and m-$Ta_5O_4I_{11}$ were obtained as black, plate-like (o-$Ta_5O_4I_{11}$) and rod-shaped (m-$Ta_5O_4I_{11}$) crystals, which are sensitive to moisture (estimated yield: ~30% (o-$Ta_5O_4I_{11}$); ~10% (m-$Ta_5O_4I_{11}$); a powder X-ray diffraction pattern is shown in Fig. S1, top). Reactions at 500 °C with a shorter reaction time of 12 hours resulted in a few black crystals of $Ta_5O_4I_{11}(TaI_5)$. Additional side phases were red TaO_2I and black, fibrous $TaOI_2$, as well as $Ta_2O_3I_4$ and $LiTa_3O_2I_{12}$ which are reported in this study.

$Nb_5O_4I_{11}$

NbI_4 (160.8 mg, 0.268 mmol), Li_2O (2 mg, 0.067 mmol) and $Li_2(CN_2)$ (7.2 mg, 0.135 mmol) were fused into a silica ampoule and heated to 400 °C with a rate of 0.1 K min^{-1}. The holding time was 24 hours before the reaction was cooled down to room temperature with a rate of 0.1 K min^{-1}. Black, plate-like crystals of $Nb_5O_4I_{11}$ were obtained at the walls of the ampoule (yield: ~10%); $NbOI_2$ and NbI_5 were sublimed to the cooler part of the ampoule, while LiI, $Li_3Nb_7O_5I_{15}$[38] and an amorphous phase were found in the hotter part at the bottom. Crystals behave sensitive in moist air. A powder X-ray diffraction pattern is shown in Fig. S1, bottom.

NbI_4 and TaI_5

were synthesised according to literature by reacting appropriate amounts of niobium or tantalum (Merck, 99.9%) with resublimed iodine (Merck, 99.999%) at 400–450 °C in evacuated quartz ampoules.[39]

$Li_2(CN_2)$

was synthesised as described before,[40] by reacting LiH (99.4%, Alfa Aesar) with melamine (≥99%) in a 6 : 1 molar ratio under argon.

Powder X-ray diffraction

All reaction products were investigated by powder X-ray diffraction (PXRD) using a StadiP diffractometer (Stoe, Darmstadt) with Ge-monochromated Cu-$K_{\alpha1}$ radiation, and a Mythen1 Detector.

Single-crystal X-ray diffraction

Data collections were performed on a Rigaku XtaLAB Synergy-S single-crystal X-ray diffractometer equipped with HyPix-6000HE detector and monochromated Mo-K_α radiation (λ = 0.71073 Å) and Cu-K_α radiation (λ = 1.54184 Å) at 150 K. X-ray intensities were corrected for absorption with a numerical method (crystal faces) using CrysAlisPro 1.171.43.121a (Rigaku Oxford Diffraction, 2024). The structures were solved by direct methods (SHELXT) and refined by full-matrix least–squares methods performed with SHELXL–2019/3 as implemented in Olex2 1.5.

EDX and SEM

Energy dispersive X-ray spectroscopy (EDX) and scanning electron microscopy (SEM) were performed on a HITACHI SU8030 scanning electron microscope with a Bruker QUANTAX 6G EDX-detector. Single crystals of o- and m-$Ta_5O_4I_{11}$ were mounted onto carbon tape under an argon atmosphere during sample preparation. For inert transfer, a vacuum transfer device, similar to the one reported by Yao *et al.*, was used.[41] In our adapted design, it consists of a steel lid with an O-ring seal (Fig. S2a). The lid is placed on top of the sample holder and evacuated within the glovebox airlock. It is then rapidly flooded with argon to create a reduced-pressure environment, ensuring an airtight seal *via* the O-ring (Fig. S2b and c). Once inserted into the SEM transfer chamber and evacuated, the internal pressure becomes equal to, or slightly higher than, the external pressure. This allows the magnetic lid to be lifted using neodymium magnets from outside the chamber (Fig. S2d).

Electrical conductivity

Conductivity measurements were performed in a Lake Shore Cryotronics CRX-6.5K probe station with a Keithley 2636B source meter unit. Rod-shaped crystals of o- and m-$Ta_5O_4I_{11}$ were contacted on a silicon substrate with 770 nm oxide layer using silver paste (Fig. S3, right) and transferred into the measuring chamber under protective gas. The conductive silver pads at each end of the crystals were connected to the circuit with gold coated tungsten tips. The chamber was kept under vacuum (<5 × 10^{-5} mbar) and the temperature was varied between 140 K and 350 K. Before each measurement,

sufficient time was allowed for the sample to reach the chosen temperature. Two-point conductivity measurements were performed by varying the applied source–drain voltage from −2 V to 2 V while detecting the current. For time-resolved photocurrent measurements, using a picosecond pulsed laser driver (Taiko PDL M1, PicoQuant) together with a laser head 779 nm (pulse length < 500 ps) the crystals were illuminated at ~55 mW cm^{-2} laser output power using the continuous wave mode under a constant bias of 1 V. The electrical measurements shown in this work had crystal dimensions (length L; width W; height H) of *o*-$Ta_5O_4I_{11}$: L = 205 μm; W = 124 μm; H = 75 μm and *m*-$Ta_5O_4I_{11}$: L = 119.4 μm; W = 32.4 μm; H = 27.3 μm.

DRIFT (diffuse reflectance infrared fourier transformation) spectroscopy

Samples were measured at room temperature under inert conditions in diffuse reflectance with a Harrick Praying Mantis attachment using a Bruker Vertex 70 infrared spectrophotometer with a deuterated triglycine sulfate (DTGS) detector and KBr beamsplitter. The background spectra were collected using pure dried KBr in powder form.

TXRF (total internal reflection X-ray fluorescence) spectroscopy

TXRF studies were performed using a S2 Picofox (Bruker AXS Microanalysis, Berlin, Germany) equipped with a Mo X-ray tube, which was operated at 50 kV and 600 μA. The measurement period for each sample was 1000 s (live time). Fitting of the resulting spectra was done using the Spectra software (Bruker Nano GmbH) in the super bias mode (maximum stripping cycles of 2000).

XPS (X-ray photoelectron spectroscopy)

XPS measurements were performed under ultra-high vacuum (UHV) conditions (8×10^{-10} mbar) using an XR50 Al-K_α standard source equipped with a PHOIBOS 100 hemispherical analyser (SPECS GmbH, Berlin, Germany). Since *o*-$Ta_5O_4I_{11}$ represents the major phase of the synthesis, the crystals used for XPS measurements were carefully selected under the optical microscope. To avoid exposure to air and prevent oxidation, the synthesised samples were mounted on a double-sided conductive carbon tape under argon atmosphere. For inert transfer into the spectrometer, a custom-built vacuum transfer device (an enlarged version of the design used for SEM/EDX) was employed. This device consists of an aluminium lid with an O-ring that seals the sample holder under reduced pressure within the glovebox airlock (Fig. S4, SI). Upon evacuation of the XPS transfer chamber, the external pressure drops below the internal pressure, causing the lid to detach and fall off, thereby revealing the sample without contact to air. The chamber is then further evacuated to UHV before transferring the sample into the measurement chamber (see Fig. S5, SI for details).

The binding energy scale was calibrated to the signal positions of Au $4f_{7/2}$ (84.0 eV), Ag $3d_{5/2}$ (368.2 eV) and Cu $2p_{3/2}$ (932.6 eV). To take charging effects into account, the acquired Ta 4f spectrum was referenced by setting the I $3d_{5/2}$ peak to a binding energy of 619 eV. Peak fitting of XPS spectra was performed using the software Unifit 2018 (Unifit Scientific Software GmbH, Leipzig, Germany).

DFT (Density functional theory)

DFT calculations were performed in the software package Abinit (v. 10).[42] The Perdew–Burke–Ernzerhof exchange–correlation functional was used with the dispersion correction of Grimme.[43,44] Calculations were performed using a plane wave basis set and the PAW formalism,[45] with an energy cut-off of 100 Ha inside the PAW spheres and 24 Ha outside. A 4 × 2 × 2 (*o*-$Ta_5O_4I_{11}$) or 3 × 2 × 2 (*m*-$Ta_5O_4I_{11}$) Monkhorst–Pack grid[46] of k-points was used to sample reciprocal space. These quantities were chosen following convergence studies. Methfessel–Paxton smearing was used to determine band occupation.[47] PAW data files were used as received from the Abinit library. The structures were relaxed to an internal pressure of 2 MPa prior to calculations of the electronic band structure.

Results and discussion

Synthesis and crystal structure

The two most stable compounds reported in the Ta–O–I system appear to be TaO_2I and $TaOI_2$, both of which were synthesised *via* transport reactions involving Ta, I_2 and Ta_2O_5 in temperature gradients of 450–550 °C.[34,35,48] In our study, we aimed to access more metal-rich compounds in this system by further reducing tantalum below the Ta(IV) oxidation state in $TaOI_2$. For this purpose we have explored Li_2CN_2 as an unconventional reduction agent, which has previously been shown its reducing nature, as demonstrated in metathesis reactions of $NiCl_2$ with Li_2CN_2, yielding elemental Ni, along with LiCl, C_3N_4 and N_2.[49]

The employment of Li_2CN_2 into the Ta–O–I system triggers reduction reactions likely above 300 °C, marked by the emergence of a violet gas phase. As the temperature exceeded 400 °C, this gas phase darkened significantly. Upon cooling, crystalline iodine was found deposited on the cooler part of the ampoule, indicating that molecular iodine is present in the gas phase, likely along with reactive precursors that contribute to the observed cluster formation.

Additionally, slightly increased pressure was observed in the ampoules, indicating the formation of N_2. Amorphous C_3N_4 was identified as a side product *via* infrared spectroscopy (see Fig. S6, SI). These findings further confirm that Li_2CN_2 acts as a reducing agent in our system, consistent with its previously reported behaviour in the reduction of $NiCl_2$ to elemental Ni.

Thermal analysis of reactions aimed to investigate the impact of Li_2CN_2 on the Ta–O–I system proved to be complex, as the reaction pathways are intricate. In addition to the observed cluster compounds (discussed in detail in this study), various crystalline and amorphous by-products were detected.

Each experiment resulted in the formation of multiple products, indicating that several reactions occurred simultaneously. The spatial distributions of these products within the reaction container suggests the occurrence of partial transport reactions along a narrow temperature gradient.

Among the consistently identified side products were LiI, $TaOI_2$ and TaO_2I, as well as two previously unreported compounds: $LiTa_3O_2I_{12}$ and $Ta_2O_3I_4$. While these compounds are not the focus of this study, their structures have been characterised by us and are briefly described as follows. Both compounds feature Ta^{5+} ions in distorted octahedral coordination environments. The structure of $LiTa_3O_2I_{12}$ forms kinked strands of $[Ta_3O_2I_{10}I_{4/2}]^-$ units which are separated by disordered lithium ions (Fig. 1 left). In $Ta_2O_3I_4$, each Ta^{5+} ion is coordinated by three oxygen and three iodide ions, forming octahedra that connect *via* corner-sharing oxygen atoms and edge-sharing iodides, with one terminal iodide per octahedra. This connectivity results in zig-zag layers (Fig. 1 right).

Efforts to minimise the amount of these side products by adjusting reactant ratios frequently resulted in lower yields of the desired cluster compounds. Likewise, prolonging the reaction duration to steer the system toward thermodynamic equilibrium did not improve reaction selectivity or reproducibility. This suggests that the cluster formation may proceed under kinetic control, potentially influenced by the side phases. Notably, the cluster compounds were consistently found in close proximity to TaO_2I, implying that this phase could serve as a precursor in the cluster-forming process.

Comparable unconventional reduction methods with Li_2CN_2 were recently reported in the Nb–O–I system, resulting in several novel niobium oxyiodides, such as the oxygen centred Nb_4OI_{12-x} clusters with $x = 0, 1, 2$.[19,37]

In extension of these findings, analogous reactions were also performed in the Ta–O–I system, yielding distinct cluster networks, referred to as *o*-$M_5O_4I_{11}$ (M = Nb, Ta), *m*-$Ta_5O_4I_{11}$, and $Ta_5O_4I_{11}(TaI_5)$, where *o* and *m* denote the orthorhombic and monoclinic polymorphs, respectively.

The crystal structure of *o*-$Ta_5O_4I_{11}$ was solved and refined from single-crystal X-ray diffraction data in the orthorhombic space group $Pmc2_1$ (No. 26). The characteristic motif of *o*-$Ta_5O_4I_{11}$ is depicted in Fig. 2: The Ta_5 cluster core adopts the motif of a distorted square pyramid. At the base of the pyramid, four μ_3-oxygen atoms bridge the edges between the metal atoms. Each of the four outer metal atoms exhibits distorted octahedral coordination by oxygen and iodide atoms with additional metal-to-metal bonding with the central metal atom on top of the pyramid (Fig. 2) with intermetallic distances given in Table 1.

The connectivity within and between clusters can be described using the notation $[(Ta_5O_4)I^i_2I^a_4I^{a-a}_{10/2}]$ where two inner (i) iodide ligands cap the edges at the apex of the distorted square-pyramidal cluster core, and four outer (a) iodides are terminally coordinated, one positioned above and three below the base of the pyramid. Additionally, ten iodide ligands are shared (10/2) between adjacent clusters, referred to as bridging outer (a–a) iodides. This notation follows the convention originally developed for describing octahedral cluster compounds.[1,7,50]

Each cluster is connected to four neighbouring clusters at its corners through bridging iodide ligands, forming extended layers expanding into the *ac*-plane. Along the *a*-axis, the Ta(2)

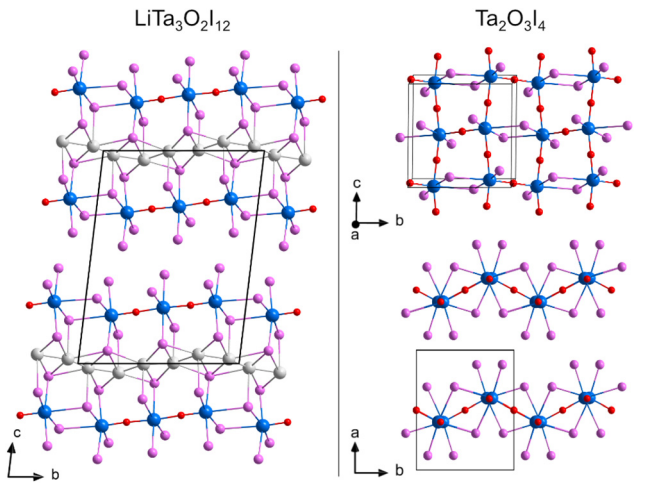

Fig. 1 Sections of the crystal structures of $LiTa_3O_2I_{12}$ (left) and $Ta_2O_3I_4$ (right). Tantalum atoms are depicted in blue, iodine pink, oxygen red and lithium grey.

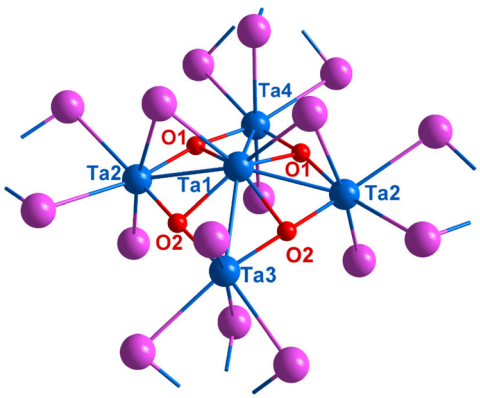

Fig. 2 Building block of isotypic $M_5O_4I_{11}$ structures (M = Nb, Ta), with the $[M_5O_4]$ cluster core displayed for M = Ta, corresponding to *o*-$Ta_5O_4I_{11}$ (iodide atoms are shown in pink).

Table 1 Comparison of selected interatomic distances and bond angles in *o*-$Ta_5O_4I_{11}$ and $Nb_5O_4I_{11}$. For atom labelling, see Fig. 2

Distance/pm; ∠/°	*o*-$Ta_5O_4I_{11}$	$Nb_5O_4I_{11}$
Intra cluster		
$M(1)$–$M(2)$	283.2(1)	285.2(1)
$M(1)$–$M(3)$	288.7(1)	287.8(4)
$M(1)$–$M(4)$	290.7(1)	290.4(4)
∠$M(2)$–$M(1)$–$M(2)$	149.3(1)	148.9(1)
∠$M(3)$–$M(1)$–$M(4)$	136.9(1)	131.3(1)
Inter cluster		
$M(2)$–$M(2)$	435.7(1)	430.1(3)
$M(3)$–$M(4)$	388.4(1)	377.5(4)

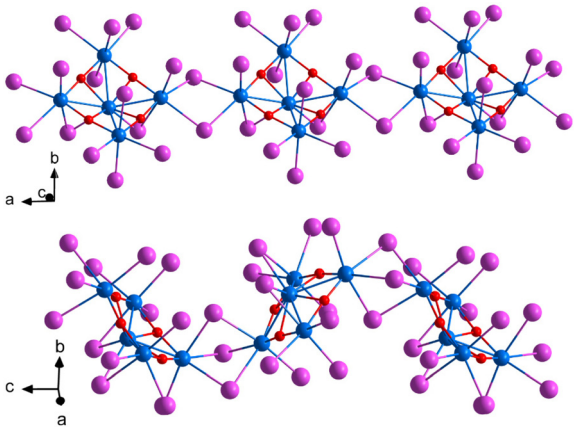

Fig. 3 Cluster connectivities in the structure of $M_5O_4I_{11}$ along *a* (top) and *c* (bottom), corresponding to *o*-$Ta_5O_4I_{11}$. *M* atoms are depicted in blue, oxygen in red and iodine in pink.

atoms are linked by two bridging iodides positioned perpendicular to an (m_x) mirror plane (Fig. 3 top). Ta(3) and Ta(4) are connected by three iodide bridges along a (2_1) screw axis that runs parallel to the *c*-axis, creating a tilted arrangement of clusters, as illustrated in Fig. 3, bottom. In the extended crystal structure, this leads to the formation of undulating layers which are separated by a van der Waals gap (Fig. 4).

A comparison of selected interatomic distances and bond angles in *o*-$Ta_5O_4I_{11}$ and the isostructural $Nb_5O_4I_{11}$ is given in Table 1. As expected, given the similarity of ionic radii of niobium and tantalum,[51] the shortest *M*–*M* bond lengths for both compounds fall within the same rang. However, the ∠*M*(3)–*M*(1)–*M*(4) bond angle, which traces the undulation of the layers along the *c*-axis, differs by around 6°. Furthermore, the inter cluster *M*(3)–*M*′(4) distance in this direction is 11 pm shorter in $Nb_5O_4I_{11}$, resulting in a slightly more pronounced corrugation of the layers.

The crystal structure of the monoclinic *m*-$Ta_5O_4I_{11}$ contains a [Ta_5O_4] cluster core similar to that found in *o*-$Ta_5O_4I_{11}$. However, the core in *m*-$Ta_5O_4I_{11}$ is less distorted due to a

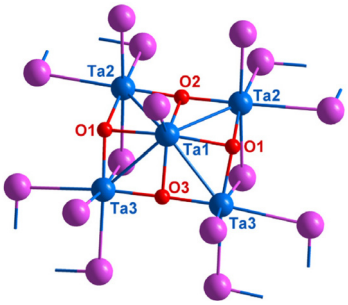

Fig. 5 Building block of the *m*-$Ta_5O_4I_{11}$ structure. Tantalum atoms are depicted in blue, oxygen atoms in red and iodine atoms in pink.

different spatial arrangement of the iodine atoms, leading to variations in how the cluster interconnect (Fig. 5). Each [$(Ta_5O_4)I^i_2I^a_5I^{a-a}_{8/2}$] cluster includes two inner (i) μ_2-bridging iodides located at the base of the pyramid, five terminal outer (a) iodides each bonded to one of the five tantalum atoms towards the pyramid's apex, and eight outer (a–a) iodides that are shared between two clusters (8/2) (see Table S1 in SI for comparison of interatomic distances).

Each cluster is interconnected with four neighbouring clusters at all four corners through two iodide bridges, forming an extended layered network. In this structure, the surrounding cluster pyramids are oriented oppositely to the central one: when the central cluster points upwards, the adjacent clusters point downwards, and *vice versa* (Fig. 6); this alternating orientation results in a sinusoidal layering pattern. These undulating layers are further separated by a van der Waals gap (Fig. 7).

The cluster network of $Ta_5O_4I_{11}(TaI_5)$ is closely related to that of *m*-$Ta_5O_4I_{11}$, but with the additional incorporation of molecular [TaI_5] units. This leads to a significant transformation of the overall structural architecture. Fig. 8 shows a section of the $Ta_5O_4I_{11}(TaI_5)$ structure (top) along with the arrangement of [$Ta_5O_4I_{11}$] layers (bottom left) and [TaI_5] units (bottom right). A closer comparison of the layer formation and

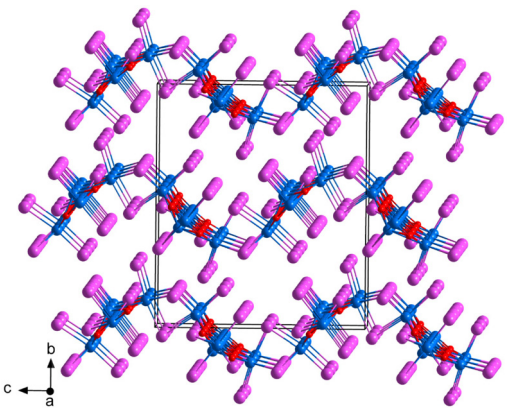

Fig. 4 Waved layer structure of $M_5O_4I_{11}$, corresponding to *o*-$Ta_5O_4I_{11}$. *M* atoms are depicted in blue, oxygen in red and iodine in pink.

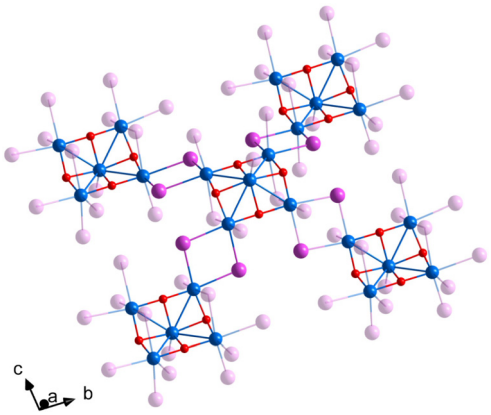

Fig. 6 Section of the *m*-$Ta_5O_4I_{11}$ structure depicting the inter-cluster connectivity within one layer. Tantalum atoms are depicted in blue, oxygen in red and iodine in pink.

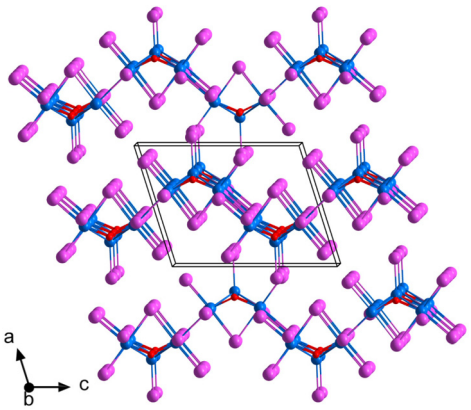

Fig. 7 Sinusoidal connectivity of clusters in the layered structure of *m*-$Ta_5O_4I_{11}$. Note that there is no connectivity between adjacent layers. Tantalum atoms are depicted in blue, oxygen in red and iodine in pink.

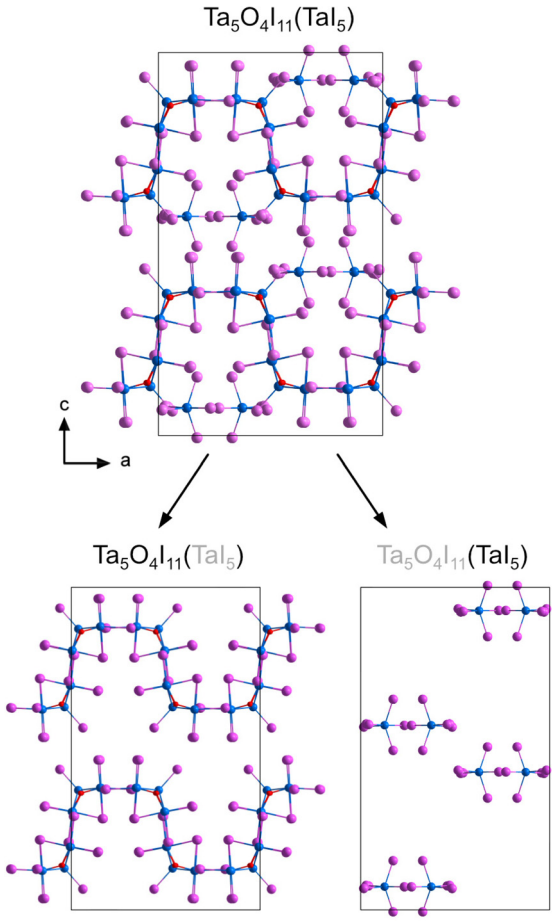

Fig. 8 Projected crystal structure of $Ta_5O_4I_{11}(TaI_5)$ (top) and segmentation of the structure into $[Ta_5O_4I_{11}]$ (left) and $[TaI_5]$, appearing as two superimposed TaI_5 units (right).

organisation in $Ta_5O_4I_{11}(TaI_5)$ (Fig. 8) and *m*-$Ta_5O_4I_{11}$ (Fig. 7) reveals clear structural differences, even though the cluster connectivity pattern $[(Ta_5O_4)I^{i}_{2}I^{a}_{5}I^{a-a}_{8/2}]$ remains the same in both structures.

Notable differences between both structures are observed in the amplitude of the sinusoidal waves of the layers and by the directional shift of these waves relative to one another. In *m*-$Ta_5O_4I_{11}$, the clusters alternate in an up-and-down fashion, whereas in $Ta_5O_4I_{11}(TaI_5)$, for each directional shift of the wave, two of the four adjacent clusters point in the same direction as the central cluster and two are inverted and point the other direction (compare Fig. 7 and Fig. 8). This more pronounced corrugation creates voids that accommodate $[TaI_5]$ molecules, which contribute to the stabilisation of the structure of $Ta_5O_4I_{11}(TaI_5)$.

This finding aligns with the observations made for the compound $Nb_7S_2I_{19} \triangleq (Nb_3SI_7)_2(NbI_5)$, which Miller and Lin described as exhibiting a synergistic relationship between the extended framework and the enclosed $[NbI_5]$ molecule.[28] In this structure, $[NbI_5]$ molecules are packed within hexagonal channels formed between the $[Nb_3SI_7]$. In contrast, when $[NbI_5]$ molecules are absent, Nb_3SI_7 adopts a van der Waals layered structure that lacks these hexagonal voids.[17]

As with the $[NbI_5]$ units in $Nb_7S_2I_{19}$, the $[TaI_5]$ molecules in $Ta_5O_4I_{11}(TaI_5)$ are incorporated as trigonal bipyramidal monomers (see Fig. 9) similar to the geometries reported for $TaCl_5$ and $TaBr_5$ in the vapour phase.[52,53] However, in the solid state, TaI_5 typically crystallises as $(TaI_5)_2$ dimers composed of edge-sharing bioctahedra.[54]

The Ta–I bond lengths of molecular $[TaI_5]$ in the structure of $Ta_5O_4I_{11}(TaI_5)$ range from 260(1) pm to 271(1) pm, with an average of 266(1) pm. This closely matches the average Nb–I distance of 267(1) pm of the NbI_5 monomers in $Nb_7S_2I_{19}$, as well as the average Ta–I distance of 267(1) pm in Ta_2I_{10}, not considering edge-sharing iodides.[54]

Although all $M_5O_4I_{11}$-based compounds share a similar penta-nuclear cluster core, they display distinct structural frameworks. These differences arise from variations in the inner (i) and outer (a) iodine ligand environments, the presence of incorporated $[TaI_5]$ molecules, as well as the cluster connectivity (a–a).

In particular, *o*-$Ta_5O_4I_{11}$ features clusters interconnected by two and three μ_2-bridging iodides at the corners (Fig. 3), resulting in shorter inter cluster Ta–Ta distances and potentially stronger electronic interactions, since *m*-$Ta_5O_4I_{11}$ clusters are only connected by two iodide bridges at all four corners (Fig. 6). This difference is expected to influence the electronic properties of the material, particularly electrical conductivity, which is discussed later in this study.

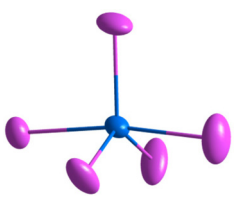

Fig. 9 Molecular $[TaI_5]$ in the structure of $Ta_5O_4I_{11}(TaI_5)$ with 80% displacement ellipsoids. Blue: Ta, pink: I.

The $[Ta_5O_4]$ cluster motive demonstrates both structural stability and geometric flexibility, as it persists across different environments and tolerates considerable distortions. However, despite these characteristics, the *o*- and *m*-modifications of $Ta_5O_4I_{11}$ are not interconvertible by thermal treatment. Heating beyond 650 °C results in decomposition and the formation of $TaOI_2$, rather than phase transition between the two forms.

For *o*-$M_5O_4I_{11}$, the structures with niobium and tantalum are isotypic. However, no analogues of *m*-$Ta_5O_4I_{11}$ or $Ta_5O_4I_{11}(TaI_5)$ could be observed for niobium. Instead, niobium forms distinct cluster types such as Nb_4OI_{12-x}, reflecting differences in cluster stability and connectivity between the two elements.[19,37]

$Ta_5O_4I_{11}$ carries six cluster electrons, but their distribution across the four short Ta–Ta bonds is not straightforward. From a formal oxidation state perspective, the four basal tantalum atoms can be assigned to Ta^{4+}, while the apical atom is considered more reduced, with an oxidation state of Ta^{3+}. To further probe this, XPS measurements are employed in the next section.

Analysis of Ta–Ta distances provide additional insights into the presence of metal–metal bonding in *o*-$Ta_5O_4I_{11}$. The average Ta–Ta bond length is approximately 286 pm, which is slightly shorter than in other tantalum halide clusters such as Ta_6I_{14} (~292 pm), Ta_3SeI_7 (~295 pm) or Ta_4SBr_{11} (~305 pm). This comparison supports the presence of bonding interactions between the tantalum atoms. Additional insight into electron distribution and bonding can be gained through ELF (Electron Localisation Function) analysis.

Scanning electron microscopy (SEM), energy dispersive X-ray spectroscopy (EDX) and total reflection X-ray fluorescence (TXRF)

When in contact with moist air, samples of $Ta_5O_4I_{11}$ show pronounced surface degradation and partial delamination (Fig. S7 in SI). To prevent this, a custom-designed vacuum transfer device was developed, enabling inert handling and transfer of samples. Details of the vessel design and operation are provided in the Experimental section and illustrated in Fig. S2 of the SI.

The scanning electron micrographs in Fig. 10 were obtained from samples transferred under inert conditions. Fig. 10 shows crystal agglomerates and surfaces morphologies of *o*-$Ta_5O_4I_{11}$ (Fig. 10a–c) and *m*-$Ta_5O_4I_{11}$ (Fig. 10d–f). The two compounds clearly exhibit different morphologies: *o*-$Ta_5O_4I_{11}$ frequently shows well defined individual layers (Fig. 10c), suggesting weaker interlayer interactions. In contrast, *m*-$Ta_5O_4I_{11}$ displays more compact, block-like surface features (Fig. 10f), indicating stronger interactions between adjacent layers.

To verify the composition, determined by X-ray diffraction, EDX measurements of multiple crystals were performed, resulting in an average Ta : O : I ratio of 5 : 4.3(5) : 10.9(3). TXRF measurements verified the Ta : I ratio to be 5 : 11.3(2).

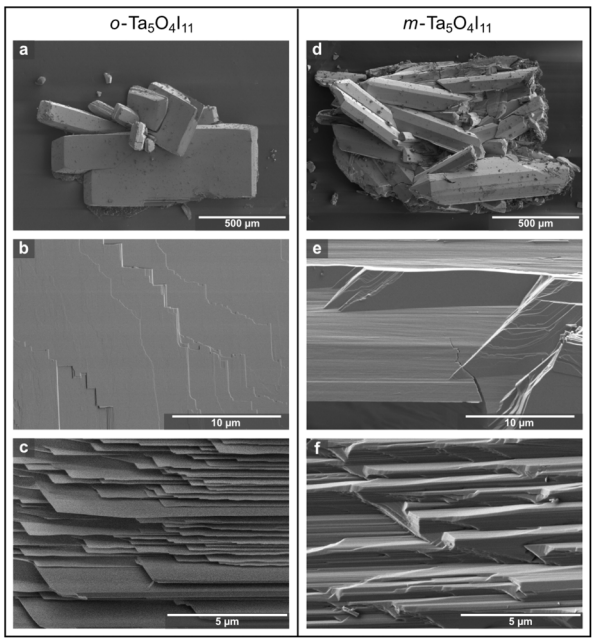

Fig. 10 Scanning electron micrographs of *o*-$Ta_5O_4I_{11}$ crystals (a–c) and *m*-$Ta_5O_4I_{11}$ crystals (d–f), showing a layered morphology.

X-ray photoelectron spectroscopy (XPS)

Further insights on the oxidation state of tantalum in *o*-$Ta_5O_4I_{11}$ were achieved using X-ray photoelectron spectroscopy (XPS).

The Ta 4f spectrum shown in Fig. 11 can be described by two doublets (Ta $4f_{7/2}$ and Ta $4f_{5/2}$), which are assigned to the oxidation states of Ta^{4+} and Ta^{3+}.[55,56] The fit parameters are summarised in Table S2 (SI). The intensity ratio of Ta^{4+} and Ta^{3+} components of 4.14 : 1 is in good agreement with the proposition of a Ta^{3+} at the central position on top of the dis-

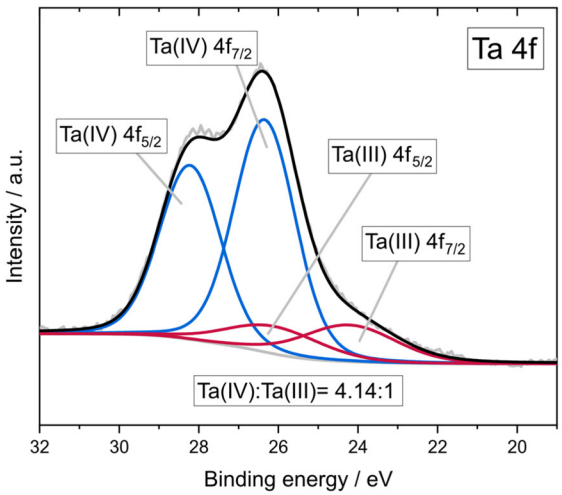

Fig. 11 XPS spectrum of Ta 4f depicting Ta(IV) and Ta(III) oxidation states in a ratio of 4.14 : 1.

torted pyramid and four Ta^{4+} at the corners of the pyramid base.

The survey spectrum in Fig. S8 (SI) reveals the presence of iodine and oxygen (notably, the additional carbon and silicon signals can be attributed to the carbon tape substrate) giving further evidence for the proposed structure.

Optical band gap determination from DRIFTS (Diffuse reflectance infrared fourier transform spectroscopy)

The absorption coefficient F was obtained using Kubelka–Munk analysis following:

$$F(R_\infty) = \frac{\alpha}{S} = \frac{(1 - R_\infty)^2}{2R_\infty},$$

where

$$R_\infty = \frac{R_{\text{sample}}}{R_{\text{standard}}}$$

is the reflectance of an infinitely thick specimen, α is the absorption and S is the scattering coefficient. For particle sizes greater than the light wavelengths measured, the scattering coefficient is understood to be approximately independent of frequency ($F(R_\infty) \sim \alpha$) and therefor $F(R_\infty)$ could be understood as a "pseudo-absorbance" coefficient.[57–63]

The band gap determination was performed on the DRIFTS data according to Zanata *et al.*[64] The energy is plotted against the absorption coefficient α and fitted with a sigmoid-Boltzmann function:

$$\alpha(E) = \alpha_{\max} + \frac{\alpha_{\min} - \alpha_{\max}}{1 + \exp\left(\frac{E - E_0^{\text{Boltz}}}{\delta E}\right)}$$

where $\alpha_{\min}$ ($\alpha_{\max}$) stands for the minimum (maximum) absorption coefficient; E_0^{Boltz} is the energy coordinate at which the absorption coefficient is halfway between $\alpha_{\min}$ and $\alpha_{\max}$; and δE is associated with the slope of the sigmoid, indicating the energy range over which most optical transitions occur.[64]

The band gap can then be calculated by following equation with $n_{\text{dir}}^{\text{Boltz}} = 0.3$ and $n_{\text{indir}}^{\text{Boltz}} = 4.3$:

$$E_g^{\text{Boltz}} = E_0^{\text{Boltz}} - n_{\text{dir/indir}}^{\text{Boltz}} \cdot \delta E$$

The optical band gaps of o-$Ta_5O_4I_{11}$ were determined to be 0.241 eV (direct) and 0.226 eV (indirect) indicating semiconducting behaviour (see Fig. S9, SI). The band gap of m-$Ta_5O_4I_{11}$ could not be measured within the detectable range of the DRIFTS setup. To further assess the electronic properties, conductivity measurement were subsequently performed.

Electrical properties

We reasoned that the structural differences in o-$Ta_5O_4I_{11}$ *vs.* m-$Ta_5O_4I_{11}$ as well as their distinct ligand environments should manifest in different electrical properties. Hence, two-point current–voltage scans of both modifications (o and m) were carried out at varying temperatures. Exemplarily results, obtained at 300 K are displayed in Fig. S3 (SI).[19,65] The measurements revealed that o-$Ta_5O_4I_{11}$ is roughly one order of magnitude more conductive than m-$Ta_5O_4I_{11}$ with typical values of 5×10^{-5} S m^{-1} to 2×10^{-4} S m^{-1} for o-$Ta_5O_4I_{11}$ *vs.* 4×10^{-6} S m^{-1} to 2×10^{-5} S m^{-1} for m-$Ta_5O_4I_{11}$.

Using the two-point conductivities obtained at different temperatures, we arrive at the Arrhenius plot in Fig. 12, indicating temperature-activated, Arrhenius type transport for both phases, which is typical for semiconductors.[66,67] From the slopes of both plots, we calculate activation energies of E_A = 0.10 eV for o-$Ta_5O_4I_{11}$ and E_A = 0.40 eV for m-$Ta_5O_4I_{11}$, respectively. Due to the poor signal strength from m-$Ta_5O_4I_{11}$ at temperatures below 240 K, additional conductivities were measured above 300 K up to 350 K to improve the fit confidence. o-$Ta_5O_4I_{11}$ was measured between 140 K–300 K.

To a first order approximation, the electrical band gap of an intrinsic semiconductor can be gauged as two times the activation energy, hence 0.2 eV for o-$Ta_5O_4I_{11}$ and 0.8 eV for m-$Ta_5O_4I_{11}$, respectively.

Both crystal species exhibit low photocurrents toward optical excitation at 779 nm illuminated with 40 mW output power. o-$Ta_5O_4I_{11}$ showed higher photocurrents around 1 nA while m-$Ta_5O_4I_{11}$ exhibited around 15 pA at 300 K (Fig. S10, SI). At lower temperatures, the photocurrent decreases gradually until it is below the noise level at ~0.1 pA.

Band structure

The spin-unpolarised electronic band structures of o-$Ta_5O_4I_{11}$ and m-$Ta_5O_4I_{11}$ were calculated using density functional theory (DFT). At the DFT level, o-$Ta_5O_4I_{11}$ is a band metal (Fig. 13), unlike the small-gap semiconductor observed in our optical and electrical measurements. Since the experimental gap of o-$Ta_5O_4I_{11}$ is small, the DFT calculations were performed with spin orbit coupling, as this could plausibly open a small gap, however this was not observed. The opening of the gap could therefore be due to electronic correlations and magnetic interactions between Ta atoms, as was determined in the related Mott insulating material Ta_4SBr_{11}.[22] However, due to the large size of the unit cell of o-$Ta_5O_4I_{11}$, computational

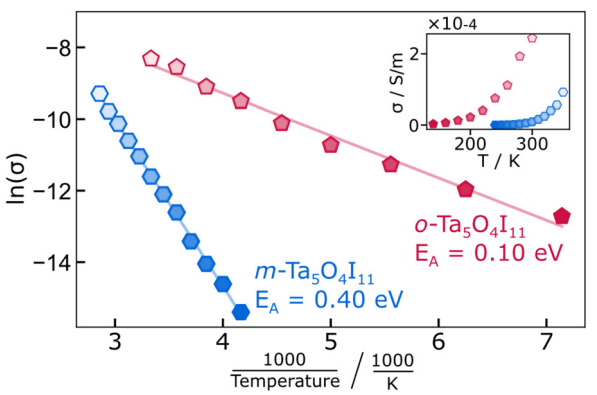

Fig. 12 Arrhenius-plot of the temperature-dependent conductivity between 140 K–300 K for o-$Ta_5O_4I_{11}$ (red) and 240 K–350 K for m-$Ta_5O_4I_{11}$ (blue). The inset shows the linear plot of conductivity *versus* temperature.

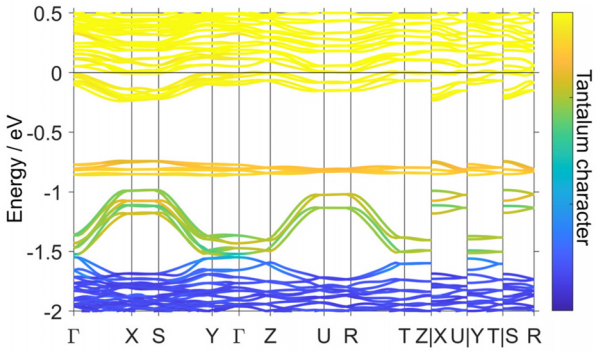

Fig. 13 Calculated electronic band structure of o-$Ta_5O_4I_{11}$, with bands coloured by their Ta character. Spin–orbit coupling was included in the calculation. Special points in and paths through reciprocal space were chosen following the literature.[68]

exploration of potential Mott behaviour was not possible in this case.

In contrast, DFT calculations showed m-$Ta_5O_4I_{11}$ to be a semiconductor with a gap of 0.4 eV (Fig. 14), in accordance with experiments. The existence of a band gap in m-$Ta_5O_4I_{11}$ is therefore most likely not due to magnetic interactions or spin–orbit coupling. Significant differences in the electronic structure and chemical bonding between o-$Ta_5O_4I_{11}$ and m-$Ta_5O_4I_{11}$ can be seen. In o-$Ta_5O_4I_{11}$, the states near the Fermi energy have predominantly Ta d character, with several distinct band manifolds being visible. The upper manifolds are nearly flat, indicating localised electrons. In m-$Ta_5O_4I_{11}$, a much greater degree of hybridisation can be seen near the Fermi level, with the valence electrons having some O and I character in addition to Ta character (see Fig. S11–S14 in the SI for details). The formation of a band gap in m-$Ta_5O_4I_{11}$ could then be ascribed to the formation of covalent bonds between Ta and other cluster atoms, whereas Ta atoms in o-$Ta_5O_4I_{11}$ are more ionic. In o-$Ta_5O_4I_{11}$, the Ta atoms would therefore be expected to behave closer to idealised Ta^{3+} and Ta^{4+}, which contain unpaired d electrons, leading to partially filled bands at the DFT level.

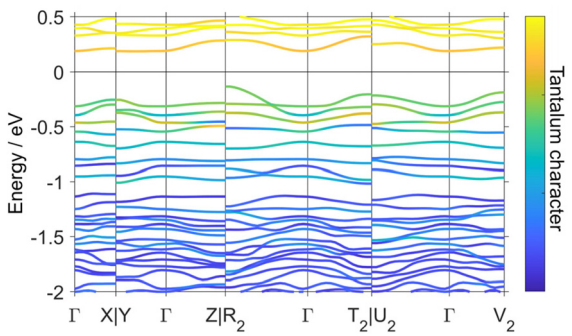

Fig. 14 Calculated electronic band structure of m-$Ta_5O_4I_{11}$, with bands coloured by their Ta character. Spin–orbit coupling was not included in the calculation. Special points in and paths through reciprocal space were chosen following the literature.[68]

Electron localisation function (ELF)

We have also calculated from DFT the electron localisation function (ELF) of o-$Ta_5O_4I_{11}$ and m-$Ta_5O_4I_{11}$, further elucidating the electronic structure and chemical bonding in these materials.[69,70] Like the band structures, the ELFs of the two polymorphs are strikingly different. The ELFs around the Ta and O atoms in o-$Ta_5O_4I_{11}$ are largely spherical, indicating ionic bonding (Fig. 15). The monoclinic modification shows

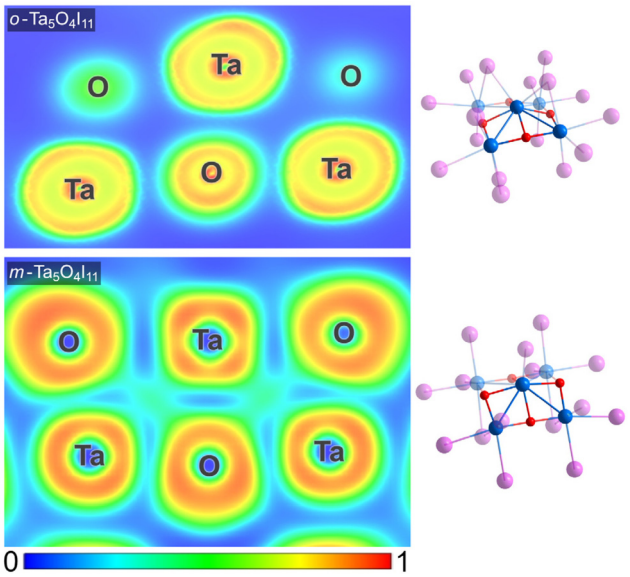

Fig. 15 Calculated ELF of o-$Ta_5O_4I_{11}$ (top) and m-$Ta_5O_4I_{11}$ (bottom), showing the presence of increased covalent bonding between Ta and O in the monoclinic phase, as demonstrated by the deviation of the shapes of the ELFs from idealised ionic spheres.

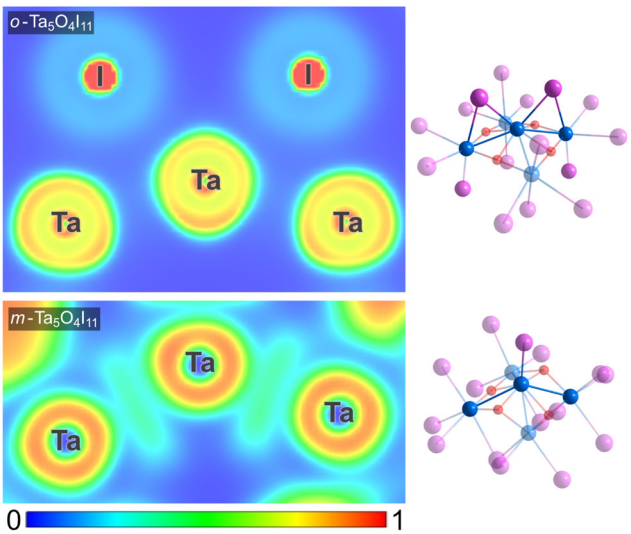

Fig. 16 Calculated ELF of o-$Ta_5O_4I_{11}$ (top) and m-$Ta_5O_4I_{11}$ (bottom), showing the presence of interstitial localised electrons in the monoclinic phase, corresponding to Ta–Ta bonds. No similar feature can be seen in the orthorhombic phase.

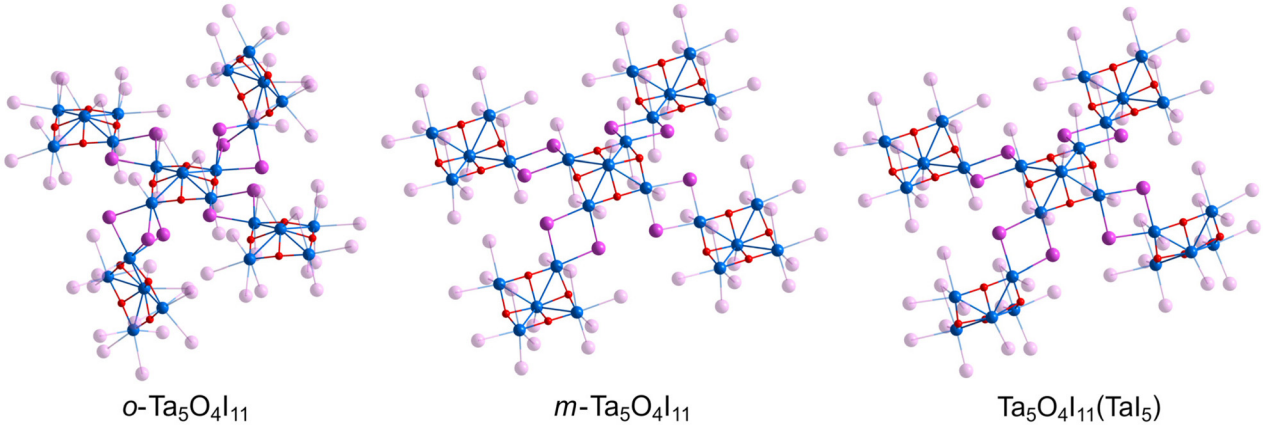

Fig. 17 Comparison of the inter cluster connectivity of *o*-$Ta_5O_4I_{11}$, *m*-$Ta_5O_4I_{11}$ and $Ta_5O_4I_{11}(TaI_5)$.

the ELFs of the atoms to be more distorted, as well as the presence of some interstitial electron density, which are indicators of covalent bonding. As Fig. 16 shows, this extra electron density lies in the planes between pairs of Ta atoms, corresponding to the formation of Ta–Ta bonds. This feature is absent in *o*-$Ta_5O_4I_{11}$, where there are instead nodal planes between the Ta atoms, again indicative of ionic interactions (compare Fig. S15 in SI).

Charge-disproportionated Ta^{3+} and Ta^{4+} ions, as seen in the XPS measurements of *o*-$Ta_5O_4I_{11}$ (Fig. 11), do not appear in our DFT calculations, where the ELFs and electron counts around the Ta atoms are nearly identical at each site. Therefore, this disproportionation could be driven by whichever factors which lead to the opening of the band gap and are not accounted for in our DFT calculations.[71]

Conclusions

Heterogeneous solid-state reactions involving an unidentified gas phase have led to the formation of the compounds $Nb_5O_4I_{11}$, *o*-$Ta_5O_4I_{11}$, *m*-$Ta_5O_4I_{11}$, and $Ta_5O_4I_{11}(TaI_5)$, all featuring an $[M_5O_4]$ cluster core. In these structures, each cluster is connected to four neighbouring clusters at the corners *via* two or three bridging iodide ligands, creating distinct extended layered networks. These connectivity patterns are summarised in Fig. 17. A common structural characteristic among these compounds is a sinusoidal layering pattern within the crystal lattice, with layers separated by van der Waals gaps. The presence of bridging outer ligands spatially separates adjacent clusters, resulting in semiconducting behaviour with low electrical conductivity primarily confined to the layers, particularly evident in both forms of $Ta_5O_4I_{11}$.

In all compounds, the $[Ta_5O_4]$ cluster core possesses six cluster electrons involved in metal–metal bonding, that could likely be localised along the four shorter metal–metal contacts between the pyramidal base and apex. According to a localised bonding model, the metal atoms in the basal plane may be assigned to Ta^{4+}, while the apical metal atom corresponds to Ta^{3+} in *o*-$Ta_5O_4I_{11}$, ensuring charge neutrality. This interpretation is supported by XPS, and it is partially consistent with charge distribution predicted by DFT calculations.

Conflicts of interest

There are no conflicts to declare.

Data availability

Data are available within the article.

The data that support the findings of this study are available on request from the corresponding author, H.-J. Meyer. Computational data are availiable from DOI: 10.5281/zenodo.17424860.

Supplementary information (SI): See DOI: https://doi.org/10.1039/d5dt02097b.

CCDC 2351105 ($Ta_5O_4I_{11}(TaI_5)$), 2380271 (*o*-$Ta_5O_4I_{11}$), 2389419 ($Ta_2O_3I_4$), 2390289 ($LiTa_3O_2I_{12}$), 2400835 ($Nb_5O_4I_{11}$) and 2424946 (*m*-$Ta_5O_4I_{11}$) and contain the supplementary crystallographic data for this paper.[72a–f]

Acknowledgements

Funding by the Deutsche Forschungsgemeinschaft through grant ME 914/32-1 and SCHE1905/9-1 is gratefully acknowledged. Computational resources were provided by the state of Baden-Württemberg through bwHPC and the DFG through grant no INST 40/467-1 FUGG (JUSTUS cluster). C. P. R. acknowledges support from the project FerrMion of the Ministry of Education, Youth and Sports, Czech Republic, co-funded by the European Union (CZ.02.01.01/00/22_008/0004591). The authors thank Ms. Elke Nadler (University Tübingen) for recording SEM images and EDX data.

References

1 H. Schäfer and H.-G. v. Schnering, *Angew. Chem.*, 1964, **76**, 833–849.
2 F. A. Cotton, *Q. Rev., Chem. Soc.*, 1966, **20**, 389–401.
3 P. Lemoine, J.-F. Halet and S. Cordier, in *Ligated Transition Metal Clusters in Solid-state Chemistry : The legacy of Marcel Sergent*, ed. J.-F. Halet, Springer International Publishing, Cham, 2019, pp. 143–190, DOI: 10.1007/430_2019_39.
4 L. Pauling, *The nature of the chemical bond and the structure of molecules and crystals*, Cornell University Press, 1949.
5 D. Bauer and H.-G. Schnering, *Z. Anorg. Allg. Chem.*, 1968, **361**, 259–276.
6 R. E. McCarley, J. Lewis and M. L. H. Green, *Philos. Trans. R. Soc. London, Ser. A*, 1982, **308**, 141–157.
7 A. Simon, H.-G. Schnering, H. Wöhrle and H. Schäfer, *Z. Anorg. Allg. Chem.*, 1965, **339**, 155–170.
8 D. G. Blight and D. L. Kepert, *Phys. Rev. Lett.*, 1971, **27**, 504–504.
9 S. L. Benjamin, Y.-P. Chang, A. L. Hector, M. Jura, W. Levason, G. Reid and G. Stenning, *Dalton Trans.*, 2016, **45**, 8192–8200.
10 D. R. Taylor, J. C. Calabrese and E. M. Larsen, *Inorg. Chem.*, 1977, **16**, 721–722.
11 P. J. Kuhn and R. E. McCarley, *Inorg. Chem.*, 1965, **4**, 1482–1486.
12 H.-G. v. Schnering, D. Vu, S.-L. Jin and K. Peters, *Z. Kristallogr. - New Cryst. Struct.*, 1999, **214**, 15–16.
13 G. Meyer, R. Wiglusz, I. Pantenburg and A.-V. Mudring, *Z. Anorg. Allg. Chem.*, 2008, **634**, 825–828.
14 F. Grahlow, M. Ströbele and H.-J. Meyer, *ICSD Commun.*, 2022, DOI: 10.25505/fiz.icsd.cc2cy0dr.
15 B. Bajan and H.-J. Meyer, *Z. Kristallogr. – Cryst. Mater.*, 1996, **211**, 818–818.
16 M. Smith and G. J. Miller, *J. Solid State Chem.*, 1998, **140**, 226–232.
17 G. V. Khvorykh, A. V. Shevelkov, V. A. Dolgikh and B. A. Popovkin, *J. Solid State Chem.*, 1995, **120**, 311–315.
18 F. Grahlow, F. Strauß, M. Scheele, M. Ströbele, A. Carta, S. F. Weber, S. Kroeker, C. P. Romao and H.-J. Meyer, *Phys. Chem. Chem. Phys.*, 2024, **26**, 11789–11797.
19 J. Beitlberger, M. Ströbele, F. Strauß, M. Scheele, C. P. Romao and H.-J. Meyer, *Eur. J. Inorg. Chem.*, 2024, **27**, e202400329.
20 H. B. Yaich, J. C. Jegaden, M. Potel, M. Sergent, A. K. Rastogi and R. Tournier, *J. Less-Common Met.*, 1984, **102**, 9–22.
21 M. N. Sokolov, A. L. Gushchin, P. A. Abramov, A. V. Virovets, E. V. Peresypkina, S. G. Kozlova, B. A. Kolesov, C. Vicent and V. P. Fedin, *Inorg. Chem.*, 2005, **44**, 8756–8761.
22 F. Grahlow, F. Strauß, P. Schmidt, J. Valenta, M. Ströbele, M. Scheele, C. P. Romao and H.-J. Meyer, *Inorg. Chem.*, 2024, **63**, 19717–19727.
23 F. A. Cotton and M. Shang, *J. Am. Chem. Soc.*, 1990, **112**, 1584–1590.
24 J. L. Seela, J. C. Huffman and G. Christou, *J. Chem. Soc., Chem. Commun.*, 1987, 1258–1260.
25 M. Ströbele, O. Oeckler, M. Thelen, R. F. Fink, A. Krishnamurthy, S. Kroeker and H.-J. Meyer, *Inorg. Chem.*, 2022, **61**, 17599–17608.
26 A. Broll, A. Simon, H.-G. von Schnering and H. Schäfer, *Z. Anorg. Allg. Chem.*, 1969, **367**, 1–18.
27 G. J. Miller, *J. Alloys Compd.*, 1995, **217**, 5–12.
28 G. J. Miller and J. Lin, *Angew. Chem., Int. Ed. Engl.*, 1994, **33**, 334–336.
29 J. Zhang and J. D. Corbett, *Inorg. Chem.*, 1995, **34**, 1652–1656.
30 K. Habermehl, A.-V. Mudring and G. Meyer, *Eur. J. Inorg. Chem.*, 2010, **2010**, 4075–4078.
31 T. C. Zietlow and H. B. Gray, *Inorg. Chem.*, 1986, **25**, 631–634.
32 J. D. Franolic, J. R. Long and R. Holm, *J. Am. Chem. Soc.*, 1995, **117**, 8139–8153.
33 M. Ströbele and H.-J. Meyer, *Dalton Trans.*, 2019, **48**, 1547–1561.
34 S. Hartwig and H. Hillebrecht, *Z. Naturforsch., B:J. Chem. Sci.*, 2007, **62**, 1543–1548.
35 M. Ruck, *Acta Crystallogr., Sect. C:Cryst. Struct. Commun.*, 1995, **51**, 1960–1962.
36 S. Hartwig and H. Hillebrecht, *Z. Anorg. Allg. Chem.*, 2008, **634**, 115–120.
37 J. Beitlberger, M. Martin, M. Scheele, P. Schmidt, M. Stroebele and H.-J. Meyer, *Dalton Trans.*, 2025, **54**, 5486–5493.
38 J. Beitlberger, M. Ströbele, P. Schmidt, C. P. Romao and H.-J. Meyer, *Dalton Trans.*, 2025, **54**, 14376–14383.
39 G. Brauer, *Handbuch der präparativen anorganischen Chemie*, Enke, 1975.
40 M. Ströbele, E. Bayat and H.-J. Meyer, *Inorg. Chem.*, 2024, **63**, 16565–16572.
41 Y. Yao, J. Liu, Z. Wang, S. Yao and F. Du, *Micron*, 2024, **187**, 103720.
42 M. J. Verstraete, J. Abreu, G. E. Allemand, B. Amadon, G. Antonius, M. Azizi, L. Baguet, C. Barat, L. Bastogne and R. Bejaud, arXiv, 2025, preprint, arXiv:2507.08578, DOI: 10.48550/arXiv.2507.08578.
43 J. P. Perdew, K. Burke and M. Ernzerhof, *Phys. Rev. Lett.*, 1996, **77**, 3865.
44 S. Grimme, J. Antony, S. Ehrlich and H. Krieg, *J. Phys. Chem.*, 2010, **132**(15), 154104.
45 M. Torrent, N. A. W. Holzwarth, F. Jollet, D. Harris, N. Lepley and X. Xu, *Comput. Phys. Commun.*, 2010, **181**(11), 1862–1867.
46 H. J. Monkhorst and J. D. Pack, *Phys. Rev. B*, 1976, **13**, 5188.
47 M. Methfessel and A. Paxton, *Phys. Rev. B:Condens. Matter Mater. Phys.*, 1989, **40**, 3616.
48 G. Brauer and A. Simon, *Handbook of Inorganic Synthesis*, 1985, vol. 5, pp. 1563–1564.
49 K. Gibson, M. Ströbele, B. Blaschkowski, J. Glaser, M. Weisser, R. Srinivasan, H.-J. Kolb and H.-J. Meyer, *Z. Anorg. Allg. Chem.*, 2003, **629**, 1863–1870.
50 B. Baján and H.-J. Meyer, *Z. Naturforsch., B:J. Chem. Sci.*, 1995, **50**, 1373–1376.
51 R. Shannon, *Acta Crystallogr., Sect. A*, 1976, **32**, 751–767.

52 H. A. Skinner and L. E. Sutton, *Trans. Faraday Soc.*, 1940, **35**, 668–680.
53 G. L. Carlson, *Spectrochim. Acta*, 1963, **19**, 1291–1307.
54 K. Habermehl, I. Pantenburg, P. Held and G. Meyer, *Z. Anorg. Allg. Chem.*, 2008, **634**, 829–831.
55 I. Perez, V. Sosa, F. G. Perera, J. T. E. Galindo, J. L. Enríquez-Carrejo and P. G. Mani-González, *Vacuum*, 2019, **165**, 274–282.
56 Y. Abbas, Y.-R. Jeon, A. S. Sokolov, S. Kim, B. Ku and C. Choi, *Sci. Rep.*, 2018, **8**, 1228.
57 W. W. Wendlandt and H. G. Hecht, *Reflectance spectroscopy*, Interscience, New York, 1966.
58 P. Kubelka, *J. Opt. Soc. Am.*, 1948, **38**, 448–457.
59 P. Kubelka and F. Munk, *Z. Tech. Phys.*, 1931, **12**, 259–274.
60 G. Kortüm and H. Koffer, *Ber. Bunsen-Ges.*, 1963, **67**, 67–75.
61 G. Kortum and J. E. Lohr, *Reflectance Spectroscopy*, Springer My Copy, UK, 1969.
62 A. B. Murphy, *Sol. Energy Mater. Sol. Cells*, 2007, **91**, 1326–1337.
63 R. López and R. Gómez, *J. Sol-Gel Sci. Technol.*, 2012, **61**, 1–7.
64 A. R. Zanatta, *Sci. Rep.*, 2019, **9**, 11225.
65 F. Fetzer, A. Maier, M. Hodas, O. Geladari, K. Braun, A. J. Meixner, F. Schreiber, A. Schnepf and M. Scheele, *Nat. Commun.*, 2020, **11**, 6188.
66 A. M. Al-Fa'ouri, O. A. Lafi, H. H. Abu-Safe and M. Abu-Kharma, *Arabian J. Chem.*, 2023, **16**, 104535.
67 M. M. A. Imran and O. A. Lafi, *Phys. B*, 2013, **410**, 201–205.
68 Y. Hinuma, G. Pizzi, Y. Kumagai, F. Oba and I. Tanaka, *Comput. Mater. Sci.*, 2017, **128**, 140–184.
69 A. D. Becke and K. E. Edgecombe, *J. Phys. Chem.*, 1990, **92**, 5397–5403.
70 A. Savin, R. Nesper, S. Wengert and T. F. Fässler, *Angew. Chem., Int. Ed. Engl.*, 1997, **36**, 1808–1832.
71 A. Walsh, A. A. Sokol, J. Buckeridge, D. O. Scanlon and C. R. A. Catlow, *J. Phys. Chem. Lett.*, 2017, **8**, 2074–2075.
72 (*a*) CCDC 2351105: Experimental Crystal Structure Determination, 2025, DOI: 10.5517/ccdc.csd.cc2jxj33; (*b*) CCDC 2380271: Experimental Crystal Structure Determination, 2025, DOI: 10.5517/ccdc.csd.cc2kwvy8; (*c*) CCDC 2389419: Experimental Crystal Structure Determination, 2025, DOI: 10.5517/ccdc.csd.cc2l6d18; (*d*) CCDC 2390289: Experimental Crystal Structure Determination, 2025, DOI: 10.5517/ccdc.csd.cc2l7938; (*e*) CCDC 2400835: Experimental Crystal Structure Determination, 2025, DOI: 10.5517/ccdc.csd.cc2ll89s; (*f*) CCDC 2424946: Experimental Crystal Structure Determination, 2025, DOI: 10.5517/ccdc.csd.cc2mdc2h.